

LETTER TO THE EDITOR

Hot and cool water in Herbig Ae protoplanetary disks

A challenge for Herschel

P. Woitke^{1,2}, W.-F. Thi³, I. Kamp⁴, and M. R. Hogerheijde⁵¹ UK Astronomy Technology Centre, Royal Observatory, Edinburgh, Blackford Hill, Edinburgh EH9 3HJ, UK² School of Physics & Astronomy, University of St. Andrews, North Haugh, St. Andrews KY16 9SS, UK³ SUPA, Institute for Astronomy, University of Edinburgh, Royal Observatory, Blackford Hill, Edinburgh EH9 3HJ, UK⁴ Kapteyn Astronomical Institute, Postbus 800, 9700 AV Groningen, The Netherlands⁵ Leiden Observatory, Leiden University, PO Box 9513, 2300 RA Leiden, The Netherlands

Received April 1, 2009; accepted May 30, 2009

ABSTRACT

The spatial origin and detectability of rotational H_2O emission lines from Herbig Ae type protoplanetary disks beyond $70\text{ }\mu\text{m}$ is discussed. We use the recently developed disk code ProDiMo to calculate the thermo-chemical structure of a Herbig Ae type disk and apply the non-LTE line radiative transfer code RATRAN to predict water line profiles and intensity maps. The model shows three spatially distinct regions in the disk where water concentrations are high, related to different chemical pathways to form the water: (1) a big water reservoir in the deep midplane behind the inner rim, (2) a belt of cold water around the distant icy midplane beyond the “snowline” $r \gtrsim 20\text{ AU}$, and (3) a layer of irradiated hot water at high altitudes $z/r = 0.1 \dots 0.3$, extending from about 1 AU to 30 AU, where the kinetic gas temperature ranges from 200 K to 1500 K. Although region 3 contains only little amounts of water vapour ($\sim 10^{-4}\text{ M}_{\text{Earth}}$), it is this warm layer that is almost entirely responsible for the rotational water emission lines as observable with Herschel. Only one ortho and two para H_2O lines with the lowest excitation energies $< 100\text{ K}$ are found to originate partly from region 2. We conclude that observations of rotational water lines from Herbig Ae disks probe first and foremost the conditions in region 3, where water is predominantly formed via neutral-neutral reactions and the gas is thermally decoupled from the dust $T_{\text{gas}} > T_{\text{dust}}$. The observation of rotational water lines does *not* allow for a determination of the snowline, because the snowline truncates the radial extension of region 1, whereas the lines originate from the region 3. Different line transfer approximations (LTE, escape probability, Monte Carlo) are discussed. A non-LTE treatment is required in most cases, and the results obtained with the escape probability method are found to underestimate the Monte Carlo results by 2% – 45%.

Key words. Astrochemistry; circumstellar matter; stars: formation; Radiative transfer; Methods: numerical; line: formation

1. Introduction

Water is one of the most important species in planet formation, disk evolution and for the origin of life. In protoplanetary disks, water can be abundant either in the gas phase or as solid ice, owing to a high sublimation temperature.

Water vapour is predicted to be abundant inside of the snowline within a few AU where densities are high and temperatures are too warm for ice formation (Agúndez et al., 2008; Glassgold et al., 2009). Indeed, observations in the near- and mid-infrared with *Spitzer* (Salyk et al., 2008; Carr & Najiita, 2008; Najiita et al., 2009; Eisner et al., 2009) reveal the presence of water vapour and other simple organic molecules (OH , C_2H_2 , HCN , CO_2). Simple modelling of the line emissions constrains the warm gas (a few 100 K) to be located inside of $r \lesssim 3\text{--}5\text{ AU}$.

The core-accretion model for planet formation is only efficient in the cold midplane of disks where dust grains are covered by water ice. Icy grains are stickier than bare silicate grains and coagulate faster into planetesimals (Ida & Lin, 2008). Liquid water is one of the prerequisites for the emergence of life on terrestrial planets. But its origin, either via release of water molecules trapped in hydrated rocks during volcanism or via the impact of comets, is still being debated (Nuth, 2008).

The lowest rotational lines of water lie in the far IR and are only observable by satellites, e.g. the *Herschel Space*

Observatory. Other recent works on rotational water lines from protoplanetary disks used X-ray models (without UV photoprocesses) to calculate the thermo-chemical disk structure on top of a pre-described density structure (Meijerink et al., 2008) and applied a multi-zone escape probability method (Poelman & Spaans, 2005, 2006) to compute the line fluxes. In this *Letter*, we use the disk code ProDiMo to compute the disk structure, temperature, and water abundance self-consistently, and discuss the prospects for detecting rotational water lines by means of the Monte Carlo code RATRAN (Hogerheijde & van der Tak, 2000).

2. The model

We used the recently developed disk code ProDiMo to calculate the thermo-chemical structure of a protoplanetary disk around a Herbig Ae type star with parameters listed in Table 1. ProDiMo combines frequency-dependent 2D dust-continuum radiative transfer, kinetic gas-phase and UV photo-chemistry, ice formation, and detailed non-LTE heating & cooling with the consistent calculation of the hydrostatic disk structure. ProDiMo does not include X-rays at the moment. X-ray to FUV luminosity ratios of Herbig Ae stars are often low $L_{\text{X}}/L_{\text{FUV}} \ll 1$ (Kamp et al., 2008), so that we assume that the FUV irradiation provides the main energy input for the disk. The model is char-

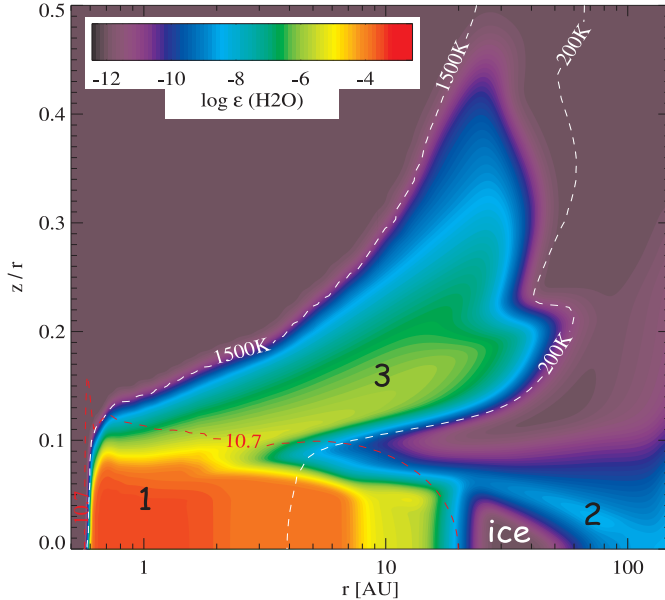


Fig. 1. Concentration of water molecules $\epsilon_{\text{H}_2\text{O}} = n_{\text{H}_2\text{O}}/n_{\langle \text{H} \rangle}$ as function of radius r and relative height above the midplane z/r for a Herbig Ae disk model. Three different regions with high water concentration can be distinguished as described in the text. The two white contours show $T_{\text{gas}} = 200$ K and 1500 K. The red contour line marks total hydrogen nuclei particle density $n_{\langle \text{H} \rangle} = 10^{10.7} \text{ cm}^{-3}$.

Table 1. Herbig Ae type disk model parameter.

quantity	symbol	value
stellar mass	M_{\star}	$2.2 M_{\odot}$
effective temperature	T_{eff}	8600 K
stellar luminosity	L_{\star}	$32 L_{\odot}$
disk mass	M_{disk}	$0.01 M_{\odot}$
inner disk radius	R_{in}	$0.5 \text{ AU}^{(1)}$
outer disk radius	R_{out}	150 AU
radial column density power index	ϵ	1.0
dust-to-gas mass ratio	ρ_d/ρ	0.01
minimum dust particle radius	a_{min}	$0.1 \mu\text{m}$
maximum dust particle radius	a_{max}	$200 \mu\text{m}$
dust size distribution power index	α_{pow}	3.5
dust material mass density ⁽²⁾	ρ_{gr}	2.5 g cm^{-3}
strength of incident ISM UV	χ^{ISM}	1
abundance of PAHs relative to ISM	f_{PAH}	0.1

(1): soft inner edge applied, see Woitke et al. (2009)

(2): dust optical constants from Draine & Lee (1984)

acterised by a high degree of consistency between the various physical, chemical, and radiative processes, where the mutual feedbacks are solved by global iterations. For more details see Woitke et al. (2009), henceforth called Paper I. Recent updates include an improved treatment of UV photorates by detailed cross sections in the calculated radiation field (see Kamp et al., 2009).

The model results in a flared disk structure with a puffed-up inner rim and a vertically extended hot atomic layer above $z/r \gtrsim 0.15 - 0.4$ from the inner rim to about $r = 20$ AU, similar to Fig. 9 in Paper I (l.h.s.), where $T_{\text{gas}} > 1000$ K due to the stellar UV-irradiation. The major difference between the T Tauri type disk discussed in Paper I and the Herbig Ae disk discussed here is that in Herbig disks, the star is much more luminous, so the dust is warmer in the midplane (here $T_{\text{dust}} > 100$ K inward of $r = 20$ AU), which prevents water ice formation.

Water molecules generally form in deeper layers, and the resulting water concentration in these layers is depicted in Fig. 1.

Table 2. Characteristics of water regions in Herbig Ae disk model.

region	r [AU]	z/r	$M_{\text{H}_2\text{O}}$ [M_{Earth}]	$\langle T_{\text{gas}} \rangle$ [K]	$\langle T_{\text{dust}} \rangle$ [K]
1	0.7 – 20	< 0.1	0.31	240	240
2	20 – 150	< 0.1	3.2×10^{-5}	38	37
3	1 – 30	0.1 – 0.3	1.1×10^{-4}	410	150

The vertical H_2O column densities in this model are found to be 10^{22} cm^{-2} at 1 AU, still 10^{19} cm^{-2} at 10 AU, but then quickly dropping below 10^{15} cm^{-2} at 30 AU and beyond.

3. Chemical pathways to water

The formation of H_2O follows different chemical pathways in the three different regions shown in Fig. 1. Two of these regions (1 and 3) have been previously identified in vertical slab models for X-ray irradiated T Tauri disks by Glassgold et al. (2009).

1) *The big inner water reservoir.* The deep midplane regions from just behind the inner rim to a distance of about 10 AU in this model host the majority of the water in the disk, see Table 2. This region is almost completely shielded from the stellar and interstellar radiation ($A_V > 10$), is still too warm for water to freeze out ($T_{\text{dust}} > 120$ K), and is characterised by large particle densities $> 10^{11} \text{ cm}^{-3}$ and thermal equilibrium between gas and dust ($T_{\text{gas}} \approx T_{\text{dust}}$). The important chemical reactions in this region are in detailed balance with their direct reverse reaction; i. e. the gas-phase chemistry is close to thermochemical equilibrium. Since H_2O is the thermodynamically most stable oxygen carrier under these conditions (after CO), the water concentration is given approximately by the element abundance of oxygen minus the fraction thereof bound in CO.

2) *The distant water belt.* Region 2 at $r \approx 20 - 150$ AU and $z/r \lesssim 0.05$ is characterised by particle densities $\sim 10^9 - 10^{10} \text{ cm}^{-3}$, temperatures $T_{\text{gas}} \approx T_{\text{dust}} \approx 30 - 100$ K, and UV-strengths χ (see Eq. (41) in Paper I) below 500. These conditions allow water to freeze out, and there is a tight equilibrium between water adsorption and photodesorption $\text{H}_2\text{O} \leftrightarrow \text{H}_2\text{O}^{\#}$, where $\text{H}_2\text{O}^{\#}$ designates water ice. The formation of gaseous water in this region is mainly controlled by the following two photoreactions



Therefore, the strength of the UV field χ controls the water vapour concentration¹. At $r = 80$ AU, χ drops from $\sim 10^3$ to virtually 0 between $z/r \approx 0.15$ and 0.02. The UV photons mostly come from the star and are scattered around the optically thick core of the disk. Water is photo-dissociated for χ that is too high, and freezes out for too low χ . The result is a thin belt of cold water vapour with concentrations in excess of 10^{-9} around the distant icy midplane. Glassgold et al. (2009) have not found region 2 in their T Tauri models, probably because their model did not include the UV photoprocesses.

3) *The hot water layer.* At distances $r \approx 1 - 30$ AU and relative heights $z/r \lesssim 0.1 - 0.3$, the model is featured by an additional layer of warm water-rich gas that is thermally decoupled from the dust $T_{\text{gas}} > T_{\text{dust}}$. The particle density is about $\sim 10^8 - 10^{10} \text{ cm}^{-3}$ in

¹ Our analysis is restricted to the case of kinetic chemical equilibrium. Thus, we cannot discuss the history of water ice formation with our model. Water ice may furthermore be photodesorbed directly into OH, see e.g. Andersson & van Dishoeck (2008).

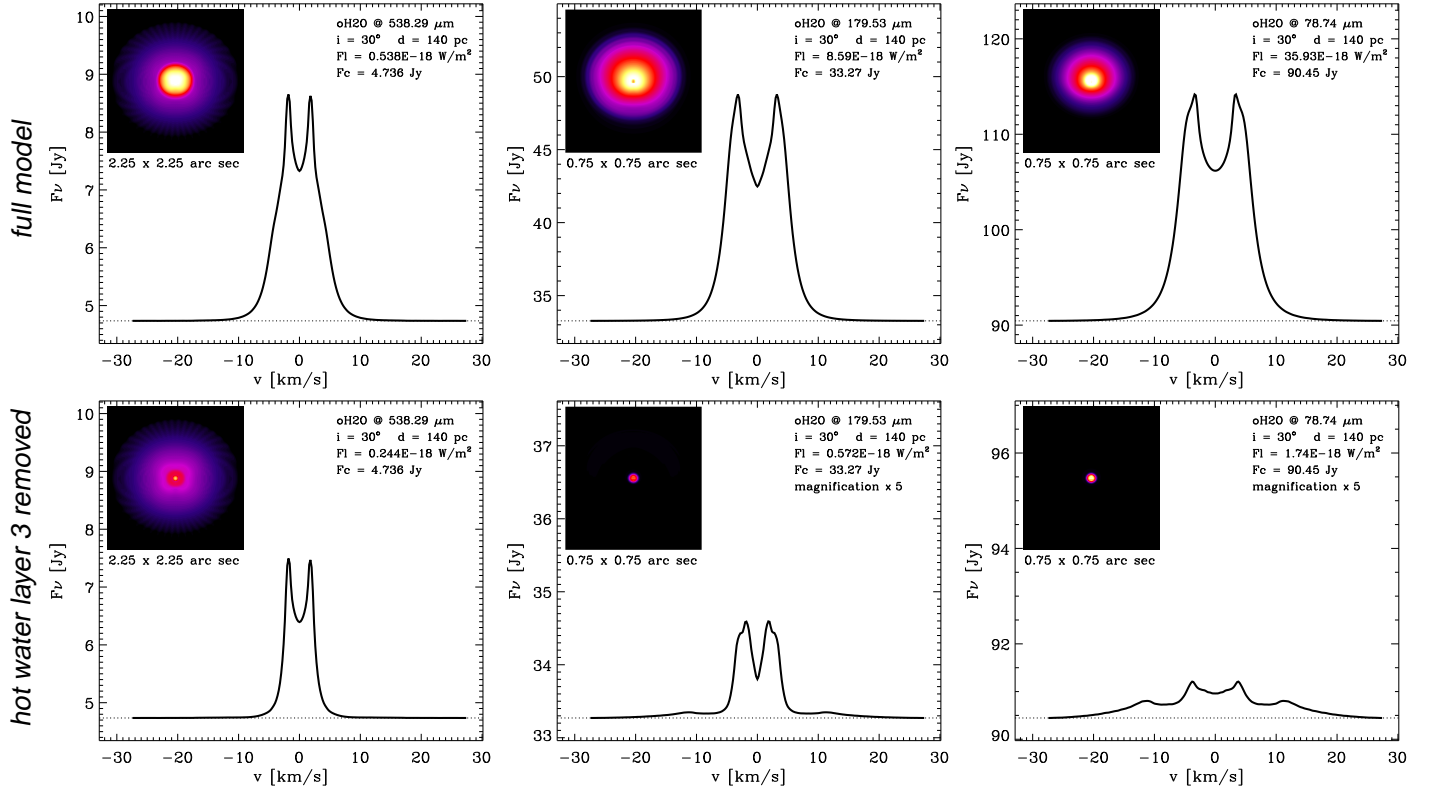


Fig. 2. Monte Carlo simulations of three ortho H₂O lines with increasing excitation energy for a distance of 140 pc and inclination 30° (infinite resolution). The inserted maps show the integrated line intensity $I(x, y) = \int I_\nu(x, y) - I_\nu^{\text{cont}}(x, y) dv$ as function of sky position (x, y) with $I_\nu^{\text{cont}}(x, y) = I_\nu(x, y)$ far away from line centre. An angular distance of 0.3" in the maps corresponds to a spatial distance of 42 AU. The first row shows the results for the full thermo-chemical input model. The second row shows the results with the water molecules being removed from region 3 (see Fig. 1). The low-excitation line on the l.h.s. is depicted on a 3× larger angular scale. The scaling of the spectral flux F_ν is partly enlarged by a factor ×5 in the lower panels as indicated. The colour-scale for the intensity maps is the same in each column.

this layer, the dust temperature 100–200 K, the gas temperature 200–1500 K, and the UV radiation field strength $\chi \approx 10^4–10^7$.

Above region 3, the high gas temperatures in combination with the direct UV irradiation from the star efficiently destroys all OH and H₂O. In region 3, the medium is shielded from the direct stellar irradiation by the puffed-up inner rim. In the shadow of the inner rim, χ drops quickly by about two orders of magnitude (the remaining UV photons are scattered stellar photons), and water forms via the following chain of surface and neutral-neutral reactions



counterbalanced by the photo-dissociation reactions OH + hν → O + H and H₂O + hν → OH + H. The reason for the minimum of the H₂O concentration between regions 3 and 1 lies in the high activation energies required for reactions (4) and (5). These neutral-neutral reactions become inefficient when the gas temperature drops below $T_{\text{gas}} \lesssim 200$ K. The radial extension of the hot water layer is restricted for the same reason. Since UV chemistry is lacking in (Glassgold et al., 2009), their water formation is counterbalanced by charge transfer reactions with H+, which also destroys OH and H₂O.

4. Spectral appearance of rotational water lines

Having calculated the density structure, the molecular abundances, the dust and gas temperatures and the continuous radiation field in the disk, we performed axisymmetric non-LTE line transfer calculations for selected rotational water lines as summarised in Table 3. The non-LTE input data for ortho (para) H₂O is taken from the Leiden LAMBDA database (Schöier et al., 2005), which includes 45 (45) levels, 158 (157) lines, and 990 (990) collisional transitions with H₂. A scaled version of the last data is also applied to collisions with H, which is essential as region 3 is partly H₂-poor and H-rich. The velocity field is assumed to be Keplerian. We add a turbulent line width of 0.15 km/s to the thermal line width throughout the disk. The ratio between para and ortho H₂O is assumed to be as in LTE.

We used three different methods of increasing complexity to calculate the water population numbers: local thermal equilibrium (LTE), a simple escape probability method (ES, see Sect. 6.1 of Paper I) and a modified version of the 2D Monte Carlo code RATRAN (Hogerheijde & van der Tak, 2000), see (Kamp et al., 2009) for modifications. The LTE and ES methods used the full 150×150 ProDiMo output directly as thermo-chemical input model. The grid size of the MC model needed to be somewhat reduced for practical reasons. We decided to run 80×80 MC models, which need about 7×10^5 photon packages to converge to a signal/noise ratio better than 5 for the worst population number in the worst cell, which takes about 13 CPU hours on a 2.66 GHz Linux machine.

To investigate the role of the hot water layer (region 3) for the spectral appearance of the rotational lines, we calculated two sets for each model. The first set includes the full chemical input model. In the second set, we artificially put the water abundance in region 3 to zero (if $n_{\text{H}} < 10^{10.7} \text{ cm}^{-3}$ and $T_{\text{gas}} > 200 \text{ K}$). The results of the two sets of MC models are compared in Fig. 2.

We generally observe double-peaked line profiles typical for rotating gas in emission. In the case of the full input model, the peak separation generally measures the radial extension of region 3 (Kepler velocity is 8.8 km/s at 25 AU in this model, inclined to 30° gives 4.4 km/s). However, the peak separation of the lowest o-H₂O excitation line (538.29 μm) and the two lowest p-H₂O excitation lines (269.27 μm and 303.46 μm, see Table 3) correspond to the full radial extent of the model, 150 AU.

The truncated model generally results in 10–20× smaller line fluxes with a broader, often unclear profile. If the water in region 3 is missing, the lines originate mainly from region 1, which is optically thick even in the continuum. Since the gas is in thermal balance with the dust in region 1 ($T_{\text{gas}} \approx T_{\text{dust}}$), the lines do not go much into emission in region 1. Again, the lowest three excitation lines behave differently, and region 2 contributes by ~30% for these lines. There is furthermore one intermittent case (o-H₂O 179.5 μm with $E_u = 114 \text{ K}$) where the truncated model reveals a small contribution of the extended region 2 with the character of low-excitation lines (middle column in Fig. 2).

All rotational water lines of the Herbig Ae disk discussed in this letter are above the 1 σ detection limit of the PACS spectrometer ($\approx 1–5 \times 10^{-18} \text{ W/m}^2$, depending on λ). The strongest water lines at 78.74 μm and 89.99 μm are above the 5 σ detection limit. However, the lines sit on a strong dust continuum, which possibly complicates the detection by Herschel.

5. LTE vs. escape probability vs. Monte Carlo

Figure 3 compares the results obtained by three different line transfer methods for the high-excitation para-H₂O line at 89.99 μm. The results for the other lines are listed in Table 3. We consider the deviations from the results of the most advanced method (MC) as a measure of the quality of the other methods. The LTE predictions are generally too high, by up to a factor of 3.5, although continuum flux, line width, and peak separation are similar. Since the densities in region 3 are lower than the critical density $\sim 10^{10} \text{ cm}^{-3}$, the levels tend to depopulate radiatively, which explains the overpredictions by LTE. Deviations between ES and MC are between 2% and 45%, and increase with excitation energy E_u . Our ES method tends to underestimate the line fluxes in general. The levels in region 3 are pumped by line radiation from distant regions in LTE that have larger line source functions. This effect is difficult, if not impossible, to be properly account for in the ES approximation.

6. Conclusions

The rotational water lines from Herbig Ae disks beyond 70 μm originate predominantly from a warm molecular layer at relative altitudes $z/r \approx 0.1–0.3$ where H₂O is formed via neutral-neutral reactions in a thermally decoupled gas ($T_{\text{gas}} > T_{\text{dust}}$). The more distant cold water around the icy midplane, where the ice is photodesorbed, contributes only to the lowest excitation lines. The peak separation of all other lines measures the radial extension of the warm molecular layer, which is about 40 AU in the discussed model. In contrast, the vast majority of water vapour in the disk is situated in the deep midplane, extending from just behind the

Table 3. Properties of rotational water lines, and calculated line fluxes $F_L = \int (F_\nu - F_\nu^{\text{cont}}) dv$ for different line transfer methods. Listed line fluxes are in units 10^{-18} W/m^2 for distance 140 pc and inclination 30°. * indicates that this line will be observed by the Herschel OT Key Programme GASPs. ES = escape probability, MC = Monte Carlo.

carrier	transition	$\lambda [\mu\text{m}]$	$A_{ul} [\text{s}^{-1}]$	$E_u [\text{K}]$	LTE	ES	MC	ES-MC
o-H ₂ O	$1_{10} \rightarrow 1_{01}$	538.29	0.0035	61	0.702	0.531	0.538	2%
o-H ₂ O	$4_{23} \rightarrow 3_{12}^*$	180.49	0.0306	194	9.27	2.32	3.39	37%
o-H ₂ O	$2_{12} \rightarrow 1_{01}^*$	179.53	0.0559	114	11.9	7.69	8.59	11%
o-H ₂ O	$3_{03} \rightarrow 2_{12}$	174.63	0.0505	197	12.7	7.47	8.88	17%
o-H ₂ O	$2_{12} \rightarrow 1_{10}$	108.07	0.256	194	54.8	11.4	17.9	44%
o-H ₂ O	$4_{23} \rightarrow 3_{12}^*$	78.74	0.484	432	94.5	24.6	35.9	37%
p-H ₂ O	$2_{02} \rightarrow 1_{11}$	303.46	0.0058	101	1.27	1.48	1.40	5%
p-H ₂ O	$1_{11} \rightarrow 0_{00}$	269.27	0.0184	53	2.40	2.22	2.09	6%
p-H ₂ O	$4_{13} \rightarrow 3_{22}^*$	144.52	0.0332	397	5.53	4.57	4.15	9%
p-H ₂ O	$3_{13} \rightarrow 2_{02}$	138.53	0.125	204	14.3	7.76	8.71	12%
p-H ₂ O	$2_{20} \rightarrow 1_{11}$	100.98	0.260	196	32.5	8.66	10.9	23%
p-H ₂ O	$3_{22} \rightarrow 2_{11}^*$	89.99	0.352	297	48.0	10.2	14.0	31%

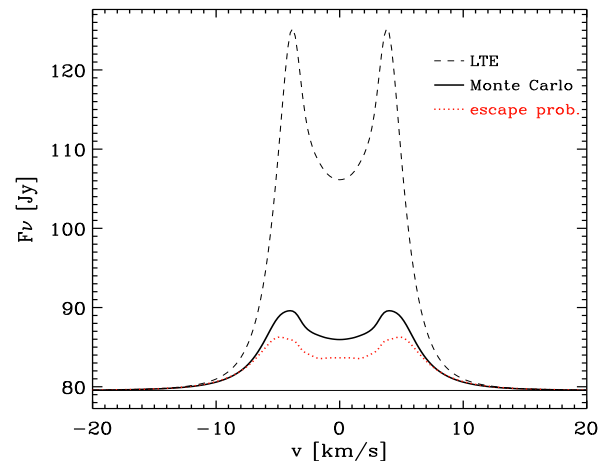


Fig. 3. Comparison between the results of different line transfer methods in application to the high-excitation para-H₂O line at 89.99 μm. The full black line rediscards the results of the Monte Carlo treatment already shown in Fig. 2, upper row, middle figure.

inner rim outward to the snowline, where water freezes out to form water ice. The gas in this massive deep water reservoir is in thermal balance ($T_{\text{gas}} \approx T_{\text{dust}}$) with optically thick dust and, therefore, no strong line emissions are produced with respect to the continuum from this deep region. Thus, no information about the position of the snowline can be deduced from the rotational water lines. A similar conclusion was reached by Meijerink et al. (2008). The line analysis generally requires a non-LTE treatment. Our escape probability method is found to underestimate the water line fluxes with respect to the more expensive Monte Carlo method by about 2%–45%.

Acknowledgements. We thank Dr. Rowin Meijerink for an open discussion about water in disks and Dr. Dieter Poelman for internal benchmark tests of different non-LTE line transfer methods.

References

- Agúndez, M., Cernicharo, J., & Goicoechea, J. R. 2008, A&A, 483, 831
- Andersson, S. & van Dishoeck, E. F. 2008, A&A, 491, 907
- Carr, J. S. & Najita, J. R. 2008, Science, 319, 1504
- Draine, B. T. & Lee, H. M. 1984, ApJ, 285, 89
- Eisner, J. A., Graham, J. R., Akeson, R. L., & Najita, J. R. 2009, ApJ, 692, 309
- Glassgold, A. E., Meijerink, R., & Najita, J. R. 2009, astro-ph 0905.4523
- Hogerheijde, M. R. & van der Tak, F. F. S. 2000, A&A, 362, 697

Ida, S. & Lin, D. N. C. 2008, *ApJ*, 685, 584

Kamp, I., Freudling, W., Robberto, M., Chengalur, J., & Keto, E. 2008, *Physica Scripta Volume T*, 130, 014013

Kamp, I., Tillig, I., Woitke, P., Thi, W.-F., & Hogerheijde, M. R. 2009, *A&A*, in prep.

Meijerink, R., Poelman, D. R., Spaans, M., Tielens, A. G. G. M., & Glassgold, A. E. 2008, *ApJ*, 689, L57

Najita, J. R., Doppmann, G. W., Carr, J. S., Graham, J. R., & Eisner, J. A. 2009, *ApJ*, 691, 738

Nuth, J. A. 2008, *Earth Moon and Planets*, 102, 435

Poelman, D. R. & Spaans, M. 2005, *A&A*, 440, 559

Poelman, D. R. & Spaans, M. 2006, *A&A*, 453, 615

Salyk, C., Pontoppidan, K. M., Blake, G. A., et al. 2008, *ApJ*, 676, L49

Schöier, F. L., van der Tak, F. F. S., van Dishoeck, E. F., & Black, J. H. 2005, *A&A*, 432, 369

Woitke, P., Kamp, I., & Thi, W.-F. 2009, *A&A*, in press, astro-ph 0904.0334, (Paper I)